# Supporting Information

# Hybrid Plasma-Thermal System for Methane Conversion to Ethylene and Hydrogen

**Rui Liu [1], Yingzi Hao [1], Tong Wang [1], Li Wang [2], Annemie Bogaerts [3], Hongchen Guo*[1], and Yanhui Yi*[1]**

[1] State Key Laboratory of Fine Chemicals, School of Chemical Engineering, Dalian University of Technology, Dalian 116024, P.R. China.

[2] College of Environmental Sciences and Engineering, Dalian Maritime University, Dalian 116026, Liaoning, China.

[3] Research group PLASMANT, Department of Chemistry, University of Antwerp, Universiteitsplein 1, BE-2610 Wilrijk-Antwerp, Belgium.

# List of contents

**Table S1 Some catalytic results of the methane non-oxidation coupling reactions [a]**

| Year | Catalysts | Reaction conditions | | | Conversion | Selectivity (%) | | | References |
|---|---|---|---|---|---|---|---|---|---|
| | | Reactants | pressure | Temperature | | $C_2H_6$ | $C_2H_4$ | $C_2H_2$ | |
| 1999 | 0.4%Ni-Ti | Pure $CH_4$ | 10 atm | 450℃ | 20% | 22% | 55% | - | 1[b] |
| 2008 | $(\equiv SiO)_2Ta$-H | Pure $CH_4$ | 50 atm | below 500℃ | 0.5% | 98% | - | - | 2- |
| 2011 | PtH-MFI | Pure $CH_4$ | 1 atm | 370℃ | 0.15% | 95% | - | - | 3 |
| 2014 | Fe@$SiO_2$ | $CH_4/N_2$=9/1 | 1 atm | 1090℃ | 48.1% | - | 48.4% | - | 4 |
| 2016 | Fe©$SiO_2$ | diluted $CH_4$ | 1 atm | 1030℃ | 20% | 65% | | | 5 |
| 2017 | PtSn/H-ZSM-5 | Pure $CH_4$ | 1 atm | 700℃ | 0.06% | - | >95% | - | 6 |
| 2017 | In/$SiO_2$ | Pure $CH_4$ | 1 atm | 825℃ | <1% | 86% | | - | 7 |
| 2018 | $Pt_1$@$CeO_2$ | $CH_4$/He=1/99 | 1 atm | 975℃ | 14.4% | 74.6% | | | 8- |
| 2018 | $Mo_2C$[B]ZSM-5 | $CH_4$/He=5/95 | 1 atm | 650℃ | 1% | | >90% | | 9 |
| 2018 | Pt-Bi/zeolite | $CH_4/N_2$ = 1/9 | 0.1 atm | 600-700℃ | 2-3% | 90% | - | - | 10 |
| 2019 | Fe–Mo/HZSM-5 | $CH_4/N_2$=9/1 | 1.5 atm | 700℃ | 2 % | 23% | 36% | - | 11 |
| 2019 | Fe©CRS | $CH_4/H_2$=1/1 | 1 atm | 1080℃ | 5.8-6.9% | 86.2% | | | 12- |
| 2019 | Fe/$SiO_2$ | $CH_4/N_2$=9/1 | 1 atm | 1000℃ | 12% | <35% | | - | 13 |
| 2020 | GaN/SBA15 | $CH_4/A_r$=5/1 | 1atm | 750℃ | 0.32% | - | 71% | - | 14 |
| 2020 | Ni-P/$SiO_2$ | Pure $CH_4$ | 1 atm | 850℃ | 0.08% | 99.9% | | - | 15 |
| 2020 | Pt@$CeO_2$ | diluted $CH_4$ | 1.5 atm | 780-910℃ | 4.3% | 60% | | | 16 |
| 2020 | $Ta^{8}O$+ | - | - | - | - | main | - | - | 17 |
| 2020 | $Fe^{II}/SiO_2$ | Pure $CH_4$ | - | 1080℃ | 3-4% | 20% | | | 18 |
| 2021 | Fe-reactor | $CH_4/N_2$=9/1 | 1 atm | 1000℃ | 7.3% | 41.2% | | | 19 |

[a] only the methane non-oxidation coupling conversion to $C_2$ products.
[b] $CH_4$ was recycled to be converted continuously for 22 h, and the produced $H_2$ was separated from reaction system to shift the reaction equilibrium.

**Table S2 .Catalytic performance of ethane dehydrogenation.**

| Catalyst | Temperature (℃) | Conversion (%) | Selectivity (%) | Reference |
|---|---|---|---|---|
| Pt-Sn/MgO | 600 | 3 | 100 | 26 |
| Pt-In/$SiO_2$ | 600 | 15 | 99 | 27 |
| Au/$SiO_2$ | 650 | 16 | 95 | 28 |
| Ni-Ga/$Al_2O_3$ | 600 | 10 | 94 | 28 |
| $Cr_2O_3/SiO_2$ | 650 | 19 | 98 | 29 |
| $Ga_2O_3/Al_2O_3$ | 650 | 28 | 93 | 30 |
| Fe/ZSM-5 | 600 | 22 | 72 | 31 |

**Table S3 .Catalytic performance of propane dehydrogenation.**

| Catalyst | Temperature (℃) | Conversion (%) | Selectivity (%) | Reference |
|---|---|---|---|---|
| $Pt_3$-Mn/$SiO_2$ | 550 | 6.8 | 95 | 32 |
| Pt-Cu/h-BN | 600 | 24 | 97 | 33 |
| Pt/In/Mg(Al)$O_x$ | 620 | 69 | 98 | 34 |
| K-$CrZr_5O_x$ | 550 | 54 | 95 | 35 |
| $GrO_x/Al_2O_3$ | 600 | 33 | 90 | 36 |
| Ce-CrOx/ $Al_2O_3$ | 630 | 86 | 78 | 37 |

**Table S4. The main reaction Scheme for the Pyrolysis of ethane.[38]**

| No. | Reaction | A, $S^{-1}$ or L $mol^{-1}$ $S^{-1}$ | E, kcal/mol |
|---|---|---|---|
| 1 | $C_2H_6 \rightarrow 2CH_3\cdot$ | $4.0 \times 10^{16}$ | 87.5 |
| 2 | $C_2H_6 + CH_3\cdot \rightarrow C_2H_5\cdot + CH_4$ | $3.8 \times 10^{11}$ | 16.5 |
| 3 | $C_2H_5\cdot \rightarrow C_2H_4 + H\cdot$ | $3.2 \times 10^{13}$ | 40 |
| 4 | $C_2H_6 + H\cdot \rightarrow C_2H_5\cdot + H_2$ | $1.0 \times 10^{11}$ | 9.7 |
| 5 | $CH_3\cdot + CH_3\cdot \rightarrow C_2H_6$ | $1.3 \times 10^{10}$ | 0 |
| 6 | $C_2H_5\cdot + CH_3\cdot \rightarrow C_3H_8$ | $3.2 \times 10^{9}$ | 0 |
| 7 | $C_2H_5\cdot + C_2H_5\cdot \rightarrow C_2H_6 + C_2H_4$ | $5.0 \times 10^{7}$ | 0 |

**Table S5. The main reaction Scheme for the Pyrolysis of propane**.[38]

| No. | Reaction | A, $S^{-1}$ or L $mol^{-1}$ $S^{-1}$ | E, kcal/mol |
|---|---|---|---|
| 1 | $C_3H_8 \rightarrow C_2H_5\cdot + CH_3\cdot$ | $2.0 \times 10^{16}$ | 84.5 |
| 2 | $C_3H_8 + CH_3\cdot \rightarrow 1\text{-}C_3H_7\cdot + CH_4$ | $3.4 \times 10^{10}$ | 11.5 |
| 3 | $C_3H_8 + CH_3\cdot \rightarrow 2\text{-}C_3H_7\cdot + CH_4$ | $4.0 \times 10^{9}$ | 10.1 |
| 4 | $C_3H_8 + C_2H_5\cdot \rightarrow 1\text{-}C_3H_7\cdot + C_2H_6$ | $1.2 \times 10^{9}$ | 12.6 |
| 5 | $C_3H_8 + C_2H_5\cdot \rightarrow 2\text{-}C_3H_7\cdot + C_2H_6$ | $8.0 \times 10^{8}$ | 10.4 |
| 6 | $1\text{-}C_3H_7\cdot \rightarrow C_2H_4 + CH_3\cdot$ | $4.0 \times 10^{13}$ | 32.6 |
| 7 | $1\text{-}C_3H_7\cdot \rightarrow C_3H_6 + H\cdot$ | $2.0 \times 10^{13}$ | 38.4 |
| 8 | $2\text{-}C_3H_7\cdot \rightarrow C_3H_6 + H\cdot$ | $2.0 \times 10^{13}$ | 38.7 |

## 1. Thermodynamic calculation of $CH_4$ pyrolysis

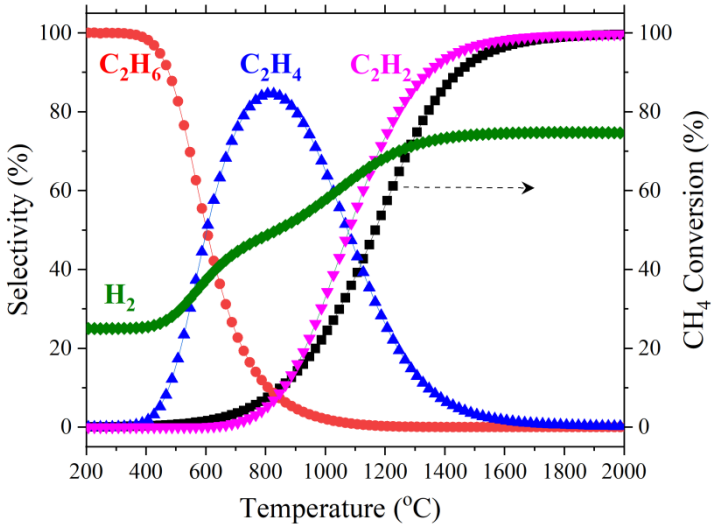


**Figure S1.** Thermodynamic equilibrium calculation of $CH_4$ pyrolysis, including $CH_4$ conversion (right y-axis) and product selectivity (left y-axis; C-based for $C_2H_6$, $C_2H_4$ and $C_2H_2$; and H-based for $H_2$).

The equilibrium composition was obtained based on the thermodynamic analysis method (database system of TheCoufal) adopted from literature.[20] In this thermodynamic calculation, the products of coke and aromatic hydrocarbons were not included, aiming to concise the trend of $C_2$ hydrocarbons selectivity. The selectivity of $C_2H_6$, $C_2H_4$ and $C_2H_2$ is based on the carbon balance, while the selectivity of $H_2$ is based on the hydrogen balance.

It can be seen from Figure S1 that at a temperature below 500 °C, $C_2H_6$ is the dominant product with nearly 100 % selectivity. With temperature increasing from 500 °C up to 800 °C, $C_2H_4$ becomes the main product at 600 °C, and the dominant product at 800 °C, with selectivity more than 80%. With temperature further increasing, the selectivity of $C_2H_4$ gradually decreases, while the selectivity of $C_2H_2$ gradually increases, and $C_2H_2$ becomes the main product at 1080 °C. For temperatures higher than 1400 °C, $C_2H_2$ becomes the dominant product with selectivity more than 90%. However, significant $CH_4$ conversion can be obtained only when the temperature is higher than 800 °C.

## 2. Experimental section

### 2.1 Experimental setup

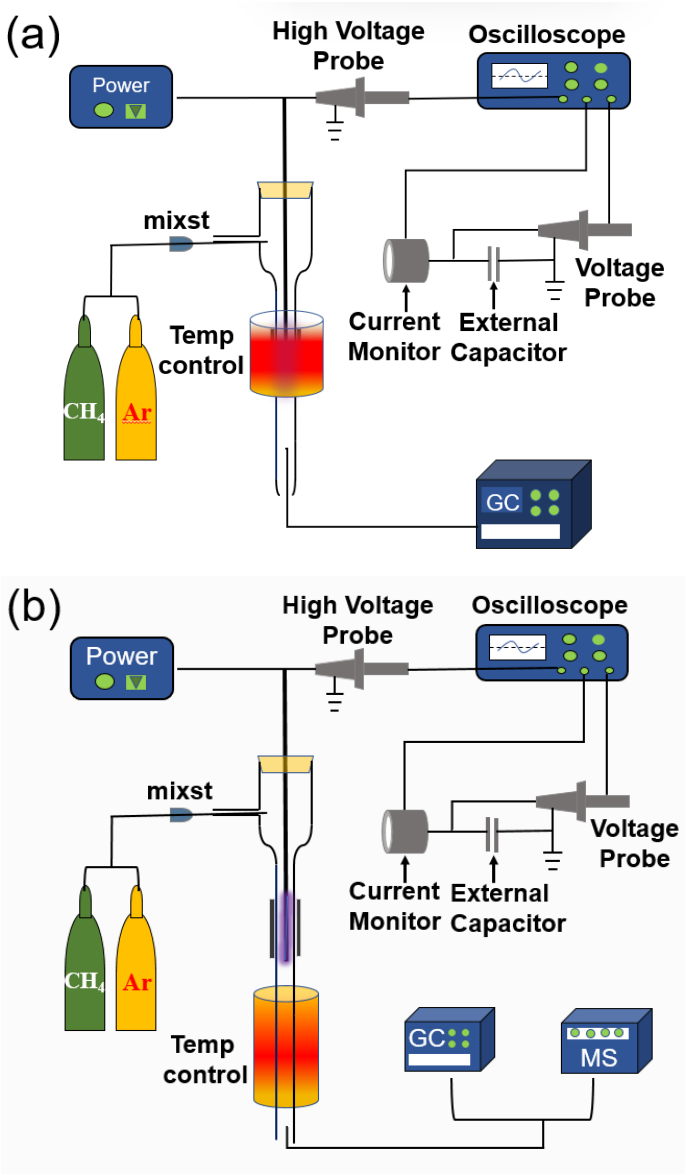


**Figure S2.** Schematic diagrams of the setup for one-stage hybrid plasma-thermal system (a) and two-stage hybrid plasma-thermal system (b) for $CH_4$ to $C_2H_4$ conversion.

All experiments were carried out in a tubular quartz reactor. The inner diameter of the quartz reactor were 8 mm. A Fe-Cr-Al wire served as the ground electrode by wrapping around the reactor. A stainless-steel rod with diameter of 2 mm was used as a high-voltage electrode. The discharge zone in the reactor was 80 mm long and the discharge gap was 3 mm. The bulk reaction temperature was controlled from 200 to 880℃ by a furnace. In the hybrid system, we controlled the temperature by manually increasing

the furnace temperature with a ramp (20 $^{o}$C or 50 $^{o}$C). In the plasma only system without external heating, we controlled the temperature by changing the discharge power. The only difference in one-stage HPTS (Figure S2a) and two-stage HPTS (Figure S2b) is that the DBD plasma and the external heating were spatially together or not. In two-stage HPTS, the heater for stage 2 placed on the same quartz tube as plasma stage 1 and the isothermal zone of stage 2 was 100 mm. Typically, the flow rate of the feedstock was 20 mL/min ($CH_4$: Ar = 1:1), which was controlled by two gas controllers. Argon is added for the purpose for enlarging the discharge and avoiding too much coking. A sinusoidal AC power supply (Suman, CTP-2000K) was connected with a transformer. The initial power and the frequency of the DBD plasma were fixed at 25 W and 14.1 kHz, respectively. The discharge parameters were collected by a digital phosphor oscilloscope (Tektronix, DPO 3012). The applied voltage of the plasma reactor was measured by a high voltage probe (1000:1, P6015A, Tektronix). The voltage across the 0.1 μF capacitor was measured by a voltage probe (10:1, TPP0101, Tektronix), which connected with the two sides of the capacitor. A current probe (Pearson 6585) was connected on the ground electrode to evaluate the current across the DBD plasma reactor. The exhaust gas is analyzed online by a mass spectrometer (HIDEN DECRA) with the Faraday detection mode, which was mainly used to make a qualitative analysis for the variation of products at three stages (plasma only, thermal cracking only and hybrid plasma-thermal system). All experiments were operated at atmospheric pressure.

### 2.2 Conversion, product analysis, energy consumption and energy efficiency

The effluent gases after the hybrid system reactor were analyzed by an online gas chromatograph (Tianmei GC7900), which was equipped with FID detector and PLOT column ($Al_2O3$, 50m × 0.53mm × 25μm). The GC was mainly used to make a quantitative analysis for the effluent gases ($CH_4$, $C_2H_2$, $C_2H_4$, $C_2H_6$, $C_3H_6$, $C_3H_8$, i-$C_4H_8$, and n-$C_4H_{10}$) after the hybrid system reactor. The concentrations of each species were calculated using an external standard method with standard curves obtained from calibrated gas mixtures. It is mentioned that the products includes other carbonaceous in the only plasma discharge or Plasma-thermal hybrid system with a low external heating temperature, but the $C_5$+ products were very little. Hence, we subsumed the $C_5$+ products into the coke. However, in the Plasma-thermal hybrid system

(> 600 ℃), there was no more products have been monitored expect our reports. It can be attributed that the majority of high carbon hydrocarbon have been cleaved at a higher temperature. The selectivity of the gas-phase products and coke are calculated based on the following equations.

$$\text{Conversion of } CH_4\ (\%) = \frac{\text{Moles of } CH_4 \text{ converted}}{\text{Moles of } CH_4 \text{ input}} \times 100\%$$

$$\text{Selectivity of } C_xH_y\ (\%) = \frac{\text{Moles of } C_xH_y \text{ produced} \times x}{\text{Moles of } CH_4 \text{ converted}} \times 100\%$$

$$\text{Selectivity of } H_2\ (\%) = \frac{\text{Moles of } H_2 \text{ produced} \times 0.5}{\text{Moles of } CH_4 \text{ converted}} \times 100\%$$

$$\text{Selectivity of coke } (\%) = 1 - \sum_{x=2}^{x=4} \text{selectivity of } C_xH_y$$

The specific energy input (SEI) is calculated using the following equation, where P(W) is the input power, F(ml/min) is the flow rate of the feed gas, and 60 is the conversion from minutes to seconds.

$$SEI(kJ/L) = 60 \times \frac{P(W)}{F(ml/min)}$$

The specific energy requirement (SER) is the energy required for full conversion of one $CH_4$ mole and is expressed as:

$$SER(kJ/mol) = \frac{SEI}{Conversion}$$

The energy consumption (EC) is the energy required for the main product, and is expressed as:

$$EC\ (kJ\ mol^{-1}) = 2 \times SEI\ /\ (Conversion \times Main\ product\ Selectivity)\ [kJ\ mol^{-1}]$$

The Energy efficiency (η, in %) is expressed as:

$$\eta\ (\%) = 100 \times \Delta H_r^{\ominus} / SER$$

Where $\Delta H_r^{\ominus}$ is the enthalpy of the $CH_4$ coupling reaction, which is taken as a function of temperature: $\Delta H_r(880℃)=251.1$ kJ/mol, $\Delta H_r(20℃)=201.5$ kJ/mol, and $\Delta H_r(180℃)=207.6$ kJ/mol, and EC is also expressed in kJ/mol.

## 3. Method of measure the temperature in Stage-one HPTS

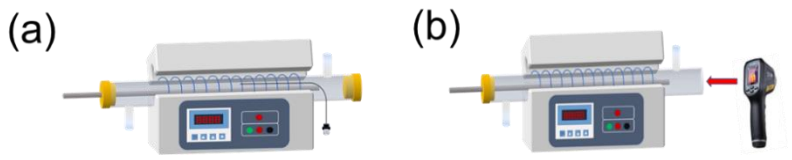


Figure S3. Schematic diagram of One-Stage hybrid plasma-thermal system.

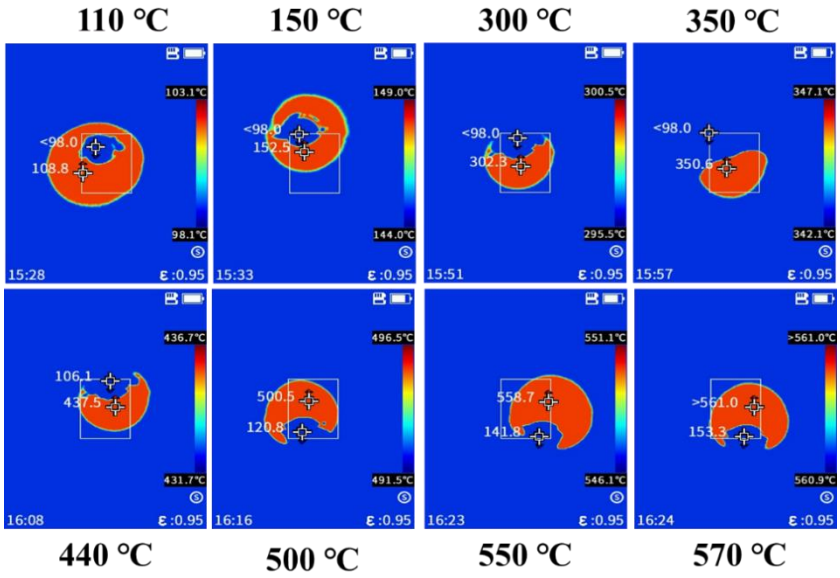


Figure S4. The temperature measured by infrared thermometer.

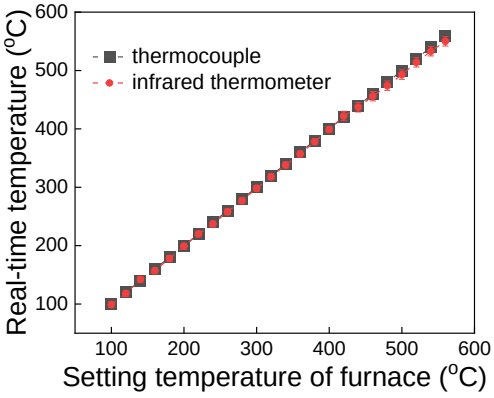


Figure S5. The real-time temperature from thermocouple and infrared thermometer varies with the setting temperature of furnace.

## 4. Discharge parameters in one-stage HPTS

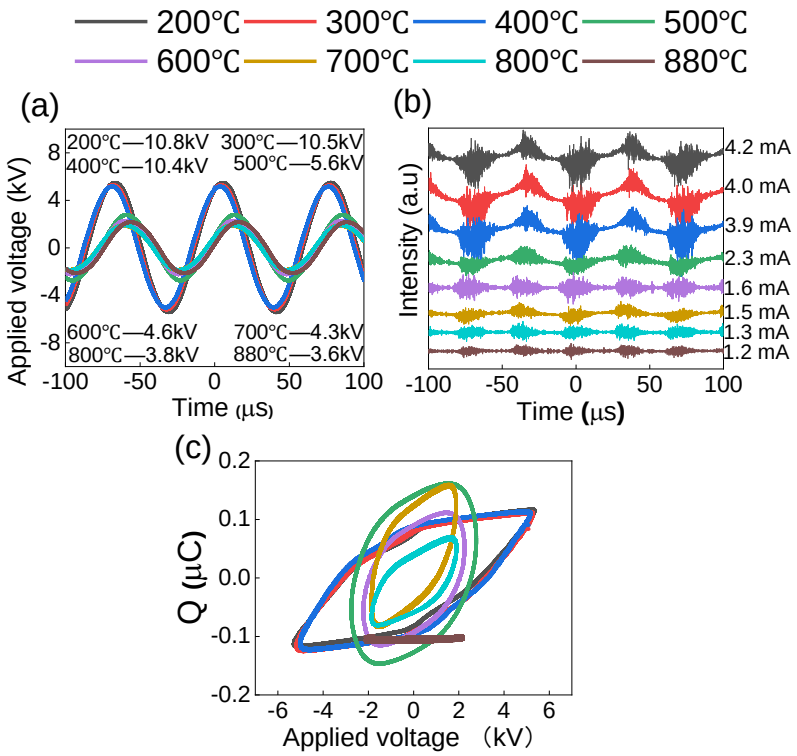


**Figure S6.** (a) Discharge voltages, (b) discharge currents and (c) Lissajous plots in the one-stage hybrid plasma-thermal system, with varying temperature adjusted by external heating.

Usually, the electron density in the plasma is proportional to the discharge current. The number of micro-discharges decreases with increasing temperature (Figure S6b). Therefore, the discharge current decreases with increasing temperature, which means that the electron density in the DBD plasma gradually reduces with increasing temperature. Thus, a smaller number of electrons will give rise to electron impact dissociation of $CH_4$, resulting in a lower $CH_4$ conversion. Additionally, the peak-peak of discharge voltage decreases with increasing temperature (Figure S3a), which means a weaker electric field was obtained at a higher temperature (E=U/d). The reduced electron density and electric field caused a lower probability of C-H bond dissociation and thus suppressed the $CH_4$ conversion at elevated temperature. In Figure S3c, with increasing temperature, the areas of the Lissajous figures gradually decreases, which indicates that the input power reduces. In summary, in the one-stage HPTS, the input power decreases with increasing the temperature.

## 5. Plasma pyrolysis of $CH_4$ in DBD without external heating

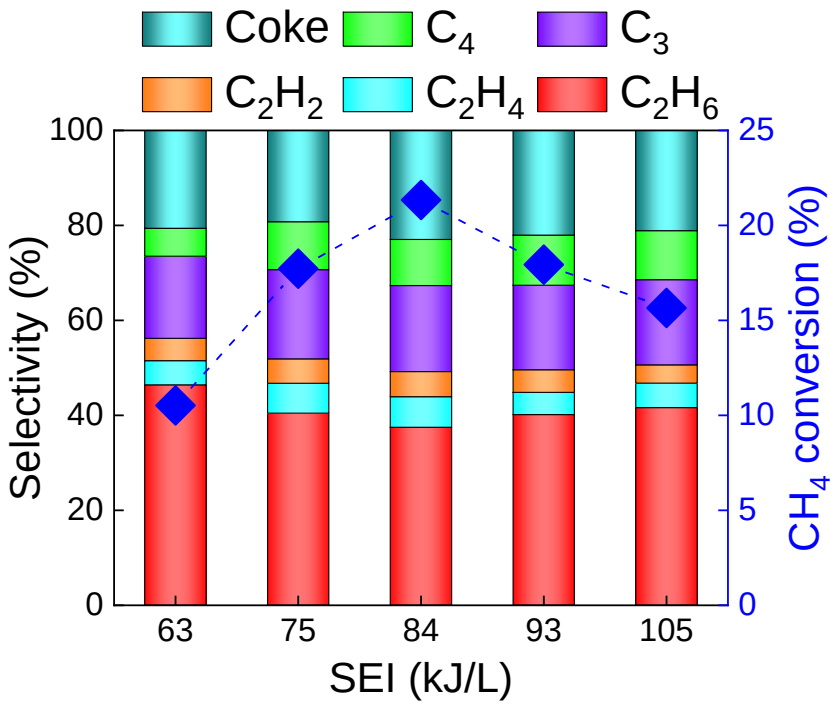


**Figure S7.** Experimental results of $CH_4$ pyrolysis by DBD plasma as a function of SEI, without external heating, at a temperature of ca. 180℃ to 400℃.

In Figure S7, the $CH_4$ conversion and product selectivities are plotted as a function of SEI applied to the discharge without external heating. At a constant flow rate of 20 ml/min, increasing SEI means higher input power.[21] Figure S4 shows that, in case of plasma only, the $CH_4$ conversion increases with rising SEI up to 84 kJ/L, but the selectivity towards $C_2H_6$ significantly drops. The same trend in the selectivity changes was found in previous studies.[22,23] However, different from previous reports,[24] as the SEI increases above 84 kJ/L, the $CH_4$ conversion drops. This may be caused by the accumulation of carbon, which inhibits the discharge and thus suppresses the dissociation and activation of $CH_4$. Importantly, $C_2H_6$ is clearly the dominant product, while $C_2H_4$ and also $C_2H_2$ are only formed in minor amounts.

## 6. $H_2$ selectivity in one-stage HPTS

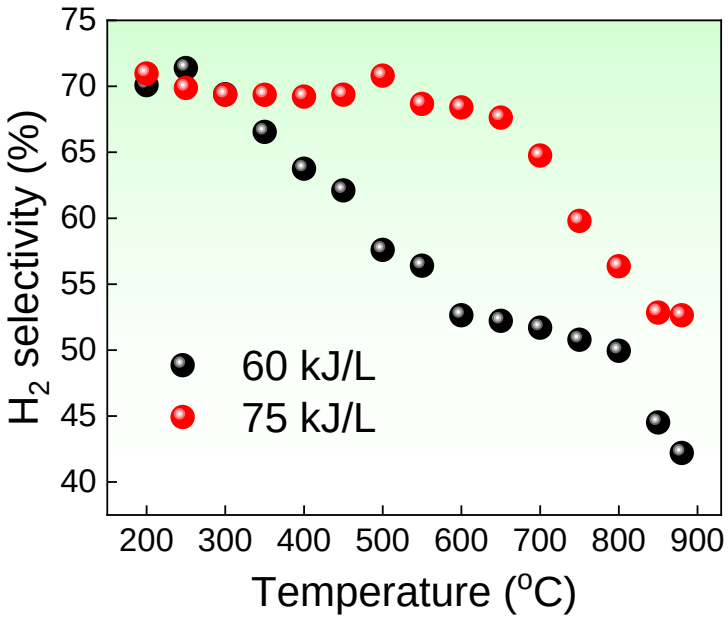


Figure S8. $H_2$ selectivity as a function of temperature in one-stage HPTS.

## 7. Thermal pyrolysis of $CH_4$

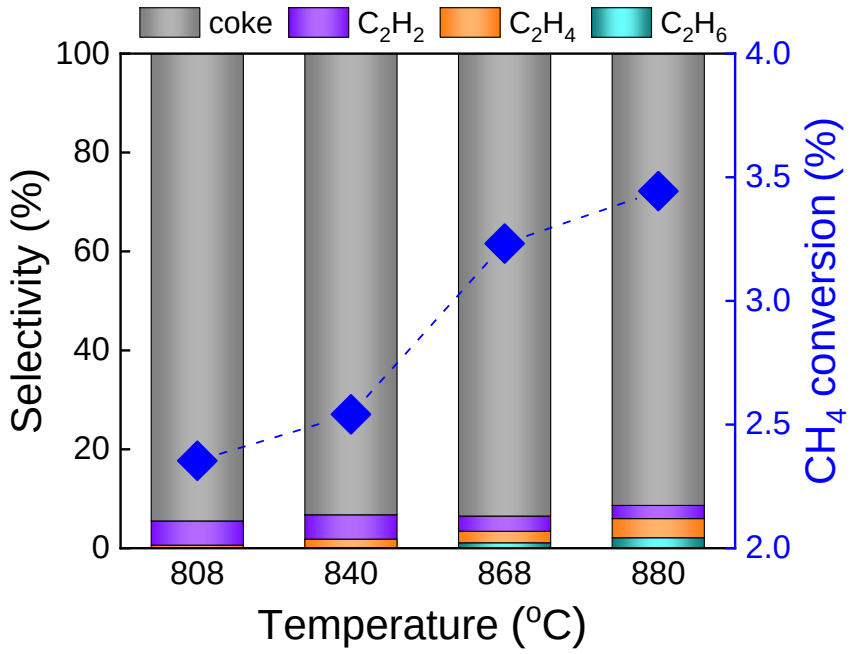


**Figure S9.** Experimental results of thermal pyrolysis of $CH_4$.

In Figure S9, a thermal pyrolysis of $CH_4$ experiment showed a $CH_4$ conversion of 2-3.5%, and around 97% of the product was coke. The conversion of $CH_4$ decreases and the the selectivity of $C_2$ increases with increasing the temperature.

## 8. Effect of SEI in one-stage HPTS

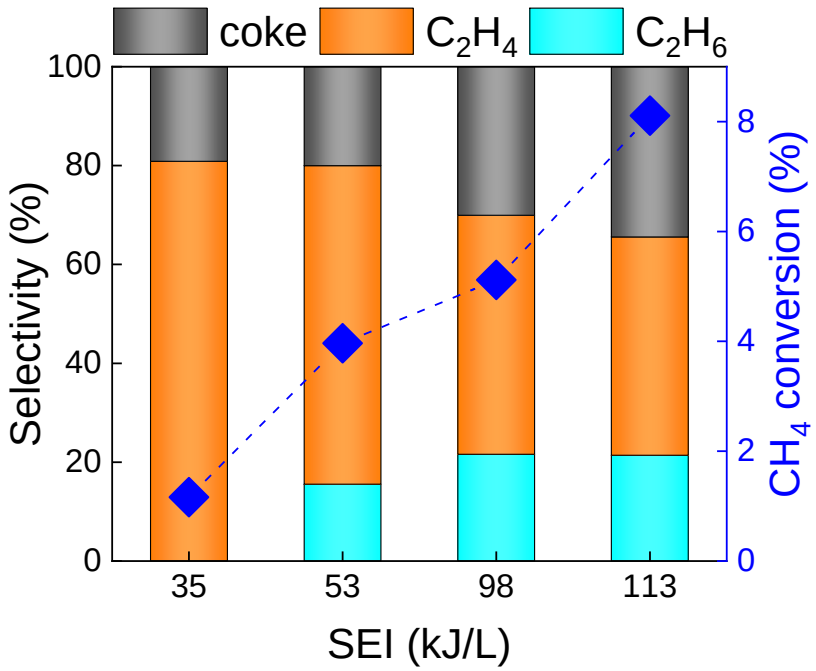


**Figure S10.** $CH_4$ conversion and product selectivity in one-stage HPTS, as a function of SEI adjusted by applying different voltages.

Figure S10 shows that the $CH_4$ conversion and $C_2H_6$ selectivity sightly increase, while the $C_2H_4$ selectivity decreases with increasing SEI at 880 ℃. It was also confirmed that the $CH_4$ conversion is inversely proportional to the selectivity of $C_2$ products with general applicability in the one-stage HPTS. That is, it is needed to establish a new reaction system.

## 9. Effect of flow rate in one-stage HPTS

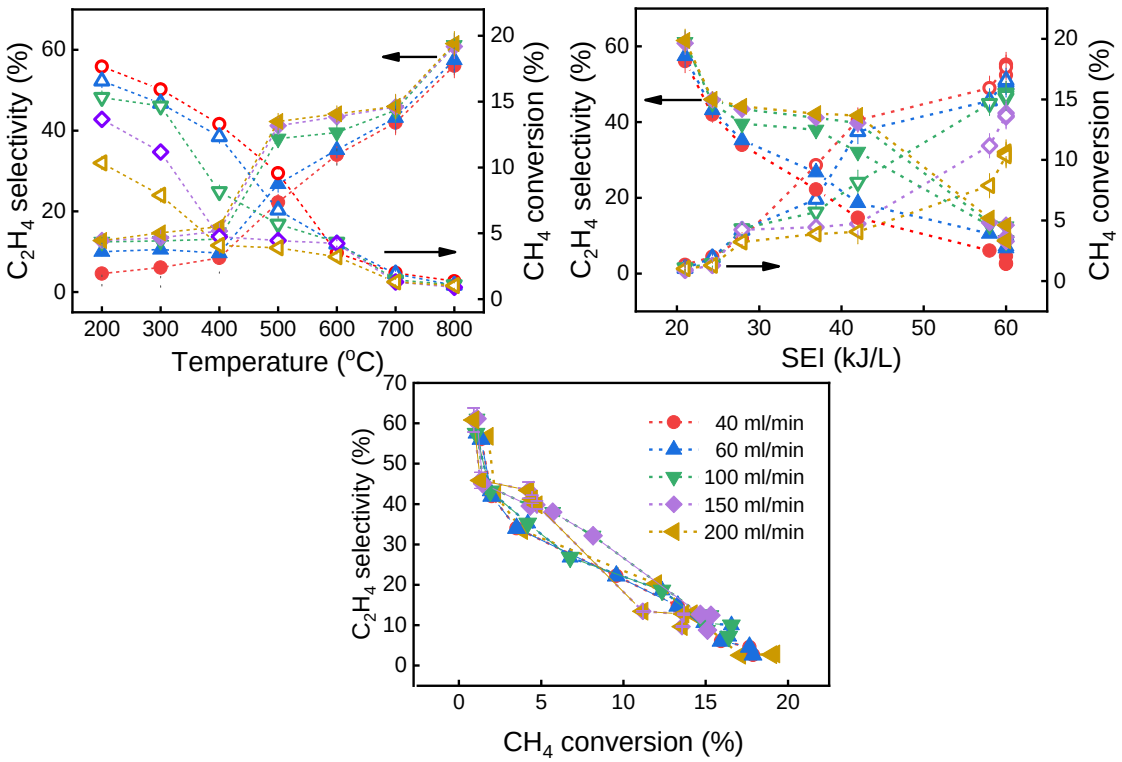


**Figure S11.** Reaction performance of one-stage HPTS for methane to ethylene conversion with different flow rates. (a) $CH_4$ conversion and $C_2H_4$ selectivity as a function of temperature; (b) $CH_4$ conversion and $C_2H_4$ selectivity as a function of SEI; (c) $CH_4$ conversion versus $C_2H_4$ selectivity.

Figure S11 shows the performance of one-stage HPTS for different flow rates. Upon increasing the external temperature, the SEI decreases, which leads to a lower $CH_4$ conversion but a higher $C_2H_4$ selectivity (Figure S11a and 11b). That is, the trade-off relationship between $CH_4$ conversion and $C_2H_4$ selectivity applies to the one-stage HPTS for methane to ethylene conversion at all the flow rates investigated (Figure S11c).

## 10. Relationship of temperature and SEI in stage 1 of two-stage HPTS

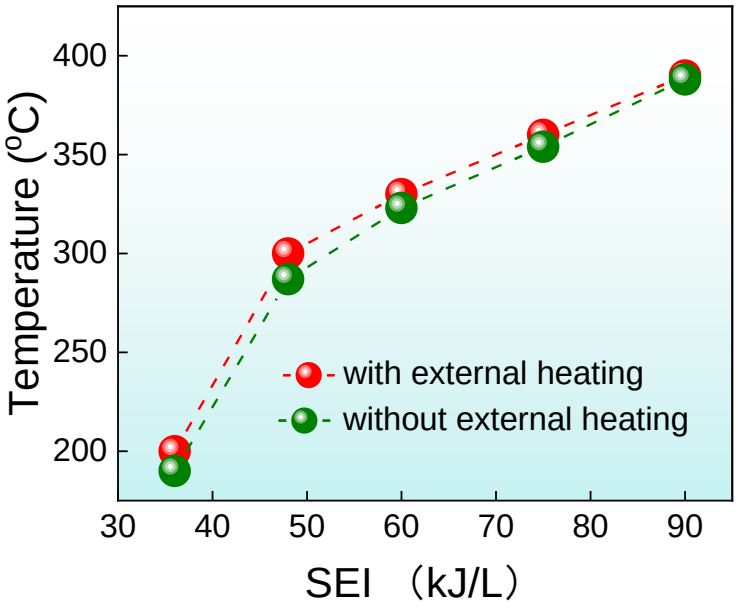


Figure S12. Effect of SEI on temperature in stage 1 of two-stage HPTS

In two-stage HPTS, the temperature of stage 1 was enhanced with increasing the SEI. The temperature of DBD reactor (stage 1) without external heating is a little lower than that with external heating. In theory, the $CH_4$ conversion increases with increasing the SEI of the stage 1. However, in experiment, the DBD discharge will be on fire with continuously increasing SEI in our setup.

## 11. Effect of flow rate in two-stage HPTS

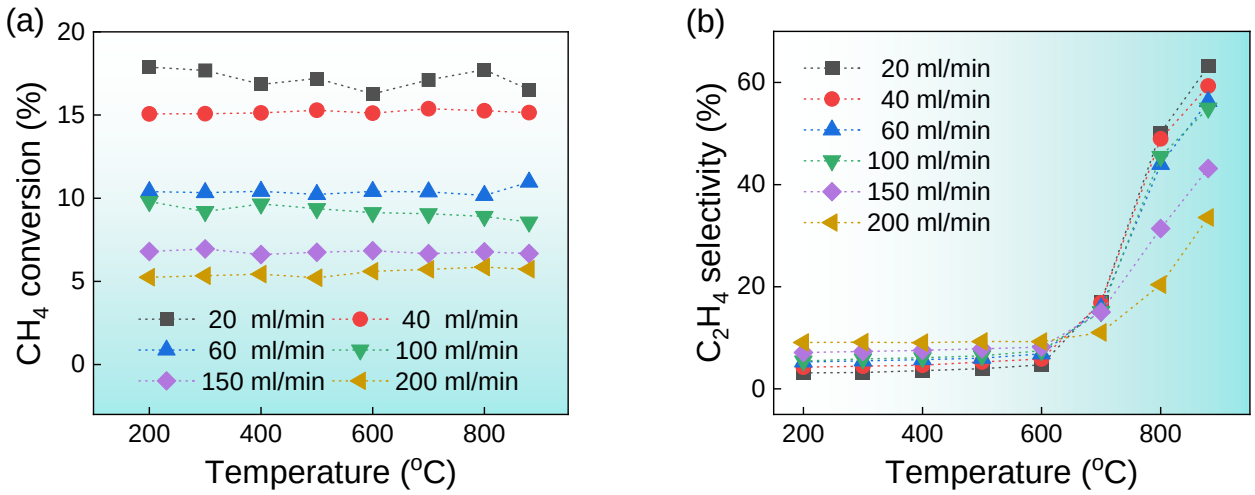


**Figure S13.** $CH_4$ conversion (a) and $C_2H_4$ selectivity (b) as a function of temperature in two-stage HPTS

## 12. Effect of the coke in two-stage HPTS

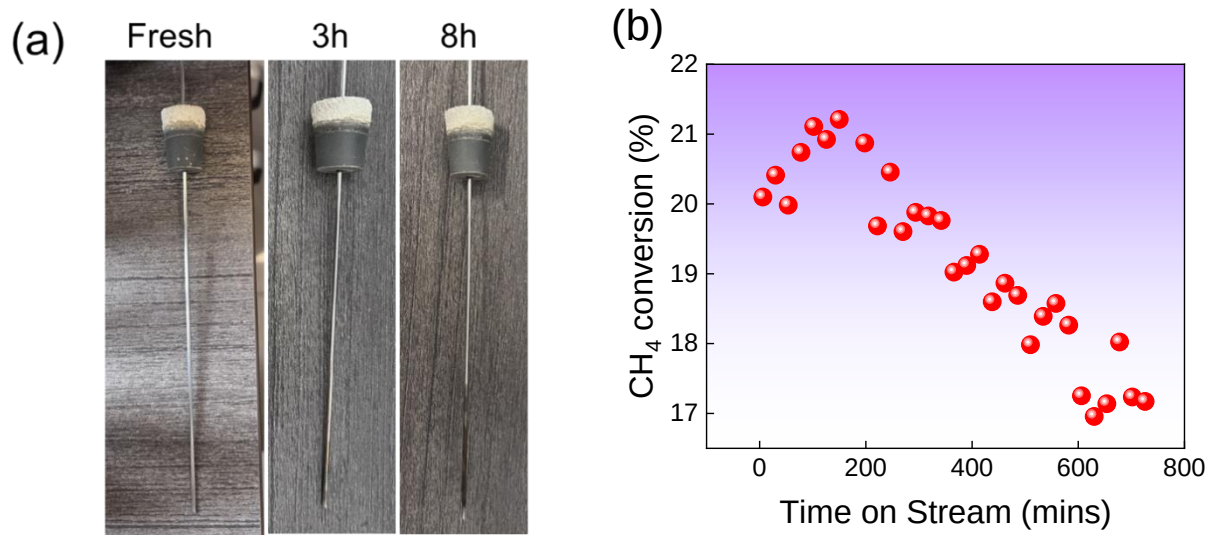


**Fgure S14**.The coke on the surface of the electrode (a) and the $CH_4$ conversion (b) varies with time on stream.

The $CH_4$ conversion decreases with the time on stream due to the accumulation of coke.

## 13. Effect of distance in two-stage HPTS

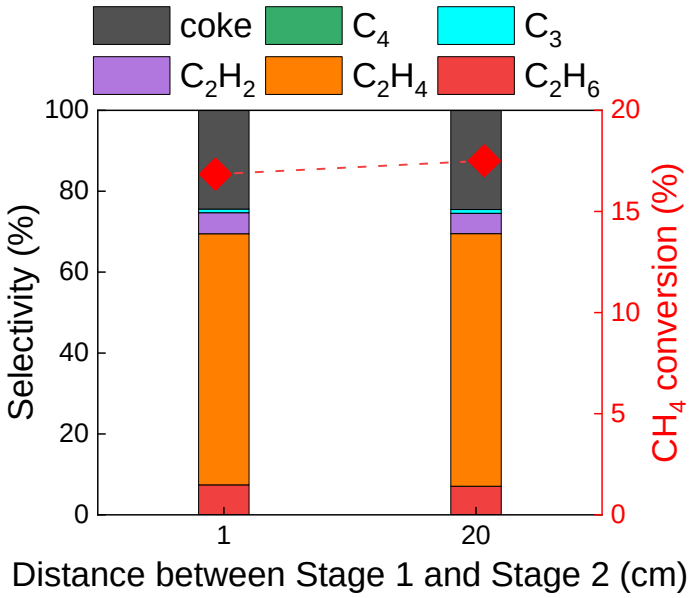


**Figure S15.** $CH_4$ conversion and product selectivity in two-stage HPTS, as a function of the distance between stage 1 and stage 2.

Figure S15 shows the effect of distance between the DBD (stage 1) and the thermal pyrolysis (stage 2) on reaction performance. However, no obvious effects were found when the distance varied from 1 cm to 20 cm.

**14. Compared with the energy consumption in different system.**

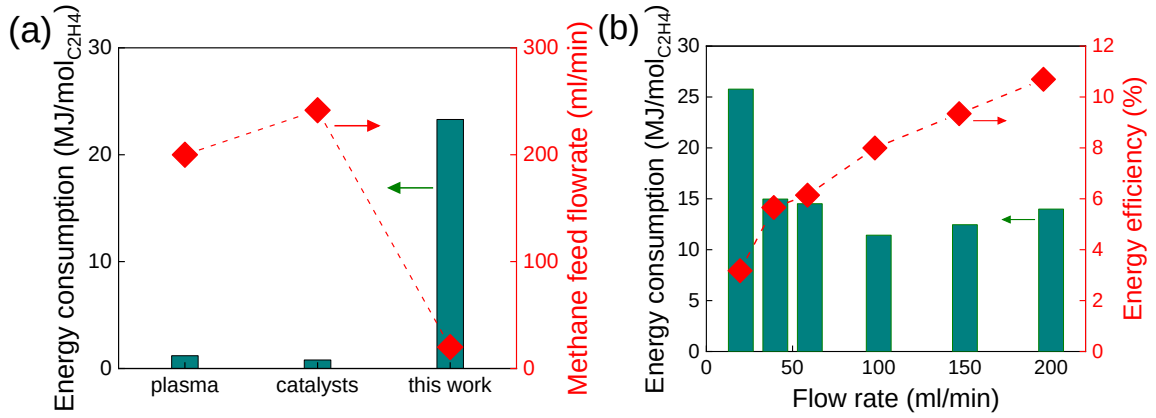


**Figure S16.** Comparison of energy consumption with the best results in literature using plasma or catalysts (a); energy consumption and energy efficiency in this two-stages HPTS with varied $CH_4$ flow rate (b).

$$EC(kJ/mol) = \frac{2\times1345\times P(W)}{F(ml/min)\times Methane\ conversion\times Main\ product\ selectivity} \quad (1)$$

$$\eta(\%) = \frac{100\times\Delta H_r^{\ominus}\times F(ml/min)\times Methane\ conversion}{1345\times P(W)} \quad (2)$$

Figure S16 a shows the energy consumption of plasma (1.2 MJ/mol),[25] traditional catalysis (0.8 MJ/mol),[4] and our two-stage HPTS (24.4 MJ/mol).Figure S16 b shows the effect of $CH_4$ flow rate on energy consumption and energy efficiency in the two stages HPTS. It can be find that energy consumption dramatically decreased, but energy efficiency obviously increased, with increasing $CH_4$ flow rate.

## 15. Thermal pyrolysis of $C_2H_6$

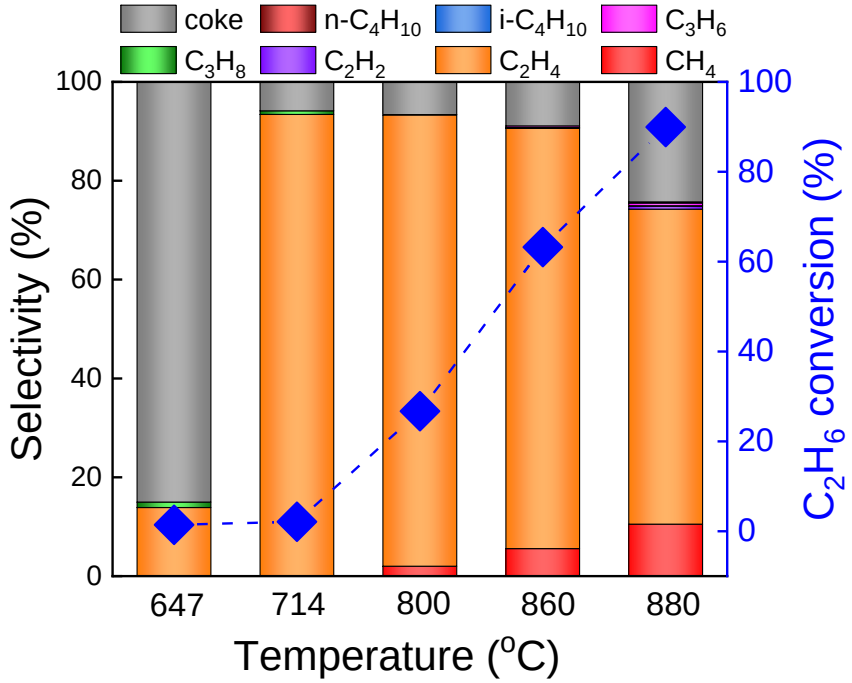


**Figure S17.** Reaction results of thermal pyrolysis of $C_2H_6$ in stage 2.

The main product of $C_2H_6$ dehydrogenation is $C_2H_4$. Some literature have reported the ethane pyrolysis, in which reaction temperatue is lower than ours (800 °C) because the catalyst has been used in these reports, as shown in Table S2.

## 16.Thermal pyrolysis of $C_3H_8$

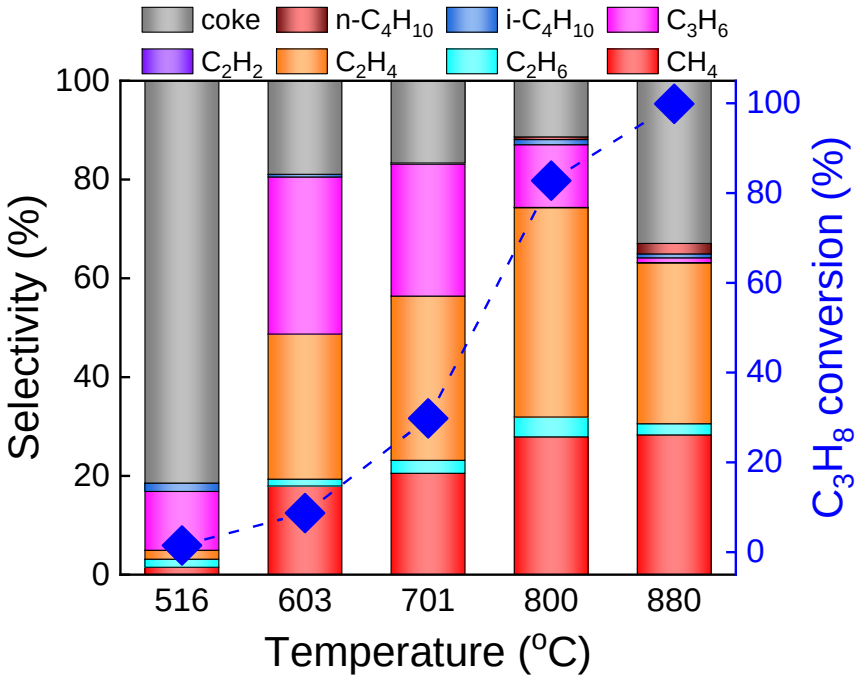


**Figure S18.** Reaction results of thermal pyrolysis of $C_3H_8$ in stage 2.

The main product of $C_3H_8$ dehydrogenation is from $C_3H_6$ to $C_2H_4$ with increasing the temperature. Some literature have reported the propane pyrolysis with a lower temperature because the catalyst has been used in these reports, as shown in Table S3.

## 17.Thermal pyrolysis of $C_4H_{10}$

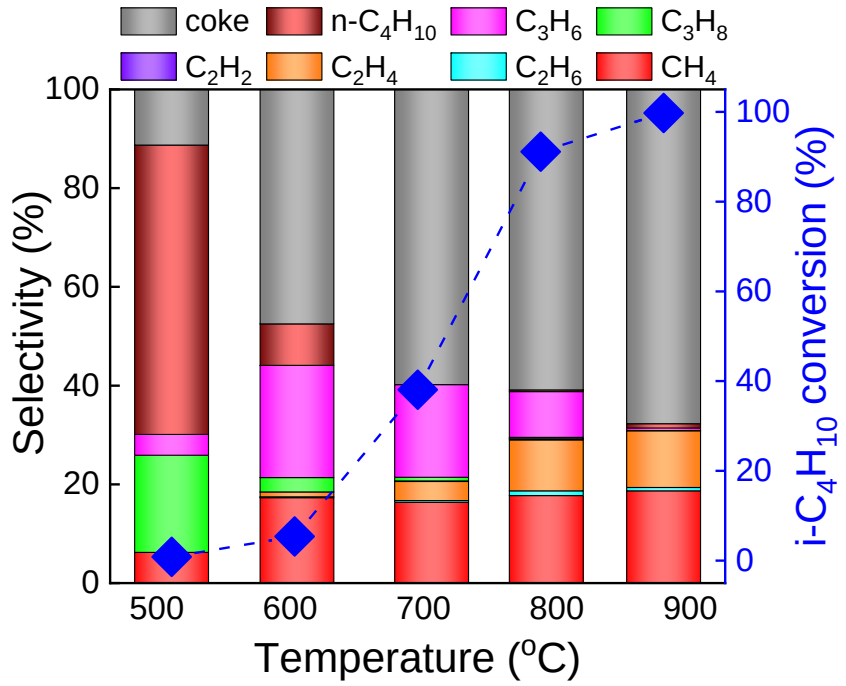


**Figure S19.** Reaction results of thermal pyrolysis of i-$C_4H_{10}$ in stage 2.

## 18. Literature Cited


[1] M. V. Tsodikov, Ye. V. Slivinskii, V. P. Mordovin, O. V. Bukhtenko, G. Colón, M. C. Hidalgo and J. A. Navío. Low temperature selective methane activation to alkenes by a new hydrogen-accumulating system. *Chem. Commun*. **1999**, 943–944.

[2] Daravong Soulivong, Se´bastien Norsic, Mostafa Taoufik, Christophe Cope´ret, Jean Thivolle-Cazat, Sudhakar Chakka, and Jean-Marie Basset. Non-Oxidative Coupling Reaction of Methane to Ethane and Hydrogen Catalyzed by the Silica-Supported Tantalum Hydride: $(\equiv SiO)_2Ta\text{-}H$. *J. Am. Chem. Soc.* **2008**, 130, 5044–5045.

[3] Dmitry B. Lukyanov, Tanya Vazhnova. Transformation of methane over platinum supported catalysts at moderate temperature. *Journal of Molecular Catalysis A: Chemical*. **2011**. 342–343.

[4] Xiaoguang Guo, Guangzong Fang, Gang Li, Hao Ma, Hongjun Fan, Liang Yu, Chao Ma, Xing Wu, Dehui Deng, Mingming Wei, Dali Tan, Rui Si, Shuo Zhang, Jianqi Li, Litao Sun, Zichao Tang, Xiulian Pan, Xinhe Bao. Direct, Nonoxidative Conversion of Methane to Ethylene, Aromatics, and Hydrogen. *Science*, **2014**, 344, 616-619.

[5] Mann Sakbodin, Yiqing Wu, Su Cheun Oh, Eric D. Wachsman, and Dongxia Liu. Hydrogen-Permeable Tubular Membrane Reactor: Promoting Conversion and Product Selectivity for Non-Oxidative Activation of Methane over an Fe©SiO2 Catalyst. *Angew. Chem*. **2016**, 128, 16383 –16386.

[6] Duygu Gerceker, Ali Hussain Motagamwala, Keishla R. Rivera-Dones, James B. Miller, George W. Huber, Manos Mavrikakis, and James A. Dumesic. Methane Conversion to Ethylene and Aromatics on PtSn Catalysts. *ACS Catal.* **2017**, 7, 2088−2100.

[7] Yuta Nishikawa, Hitoshi Ogihara, and Ichiro Yamanaka. Liquid-Metal Indium Catalysis for Direct Dehydrogenative Conversion of Methane to Higher Hydrocarbons. *ChemistrySelect*. **2017**, 2, 4572 – 4576.

[8] Pengfei Xie, Tiancheng Pu, Anmin Nie, Sooyeon Hwang, Stephen C. Purdy, Wenjian Yu, Dong Su, Jeffrey T. Miller, and Chao Wang. Nanoceria-Supported Single-Atom Platinum Catalysts for Direct Methane Conversion. *ACS Catal*. **2018**, 8, 4044−4048.

[9] Huibo Sheng, Edward P. Schreiner, Weiqing Zheng, and Raul F. Lobo. Non-oxidative Coupling of Methane to Ethylene Using Mo2C/[B]ZSM-5. *ChemPhysChem.* **2018**, 19, 504-511.

[10] Yang Xiao and Arvind Varma. Highly Selective Nonoxidative Coupling of Methane over Pt-Bi Bimetallic Catalysts. *ACS Catal*. **2018**, 8, 2735−2740.

[11] David Bajec, Andrii Kostyniuk, Andrej Pohar, Blaž Likozar. Nonoxidative methane activation, coupling, and conversion to ethane, ethylene, and hydrogen over Fe/HZSM-5, Mo/HZSM-5, and Fe–Mo/HZSM-5 catalysts in packed bed reactor. *Int J Energy Res*. **2019**, 43, 6852–6868.

[12] Seung Ju Han, Sung Woo Lee, Hyun Woo Kim, Seok Ki Kim, and Yong Tae Kim. Nonoxidative Direct Conversion of Methane on Silica-Based Iron Catalysts: Effect of Catalytic Surface. *ACS Catal.* **2019**, 9, 7984−7997.

[13] Su Cheun Oh, Emily Schulman, Junyan Zhang, Jiufeng Fan, and Dongxia Liu. Direct Non-oxidative Methane Conversion in a Millisecond Catalytic Wall Reactor. *Angew. Chem*. **2019**, 58,7083-7086.

[14] Kanchan Dutta , Vishnu Chaudhari , Chao-Jun Li , Jan Kopyscinski. Methane conversion to ethylene over GaN catalysts. Effect of catalyst nitridation. *Applied Catalysis A, General*. **2020**, 595, 117430.

[15] Arnoldus Lambertus Dipu, Shunya Ohbuchi, Yuta Nishikawa, Shoji Iguchi, Hitoshi Ogihara, and Ichiro Yamanaka. Direct nonoxidative conversion of methane to higher hydrocarbons over silica supported nickel phosphide catalyst. *ACS Catal.* **2020**, 10, 375-379.

[16] David Bajec, Andrii Kostyniuk, Andrej Pohar, Blaž Likozar. Micro-kinetics of non-oxidative methane coupling to ethylene over Pt/CeO2 catalyst. *Chemical Engineering Journal*. **2020**, 396, 125182.

[17] Nikita Levin, Jozef Lengyel, Jan F. Eckhard, Martin Tschurl, and Ueli Heiz. Catalytic Non-Oxidative Coupling of Methane on $Ta_8O_2^+$. J. *Am. Chem. Soc*. **2020**, 142, 5862−5869.

[18] PetrŠot, Mark A. Newton, Dirk Baabe, Marc D. Walter, Alexander P. van Bavel, Andrew D. Horton, Christophe Copéret, and Jeroen A. van Bokhoven. Non-oxidative Methane Coupling over Silica versus Silica-Supported Iron(II) Single Sites. *Chem. Eur. J*. **2020**, 26, 8012 – 8016.

[19] Jianqi Haoa, Pierre Schwacha, Lulu Li, Xiaoguang Guo, Junben Weng, Hailei Zhang, Hao Shen, Guangzong Fang, Xin Huang, Xiulian Pan, Chunlei Xiao, Xueming Yang, Xinhe Bao. Direct experimental detection of hydrogen radicals in non-oxidative methane catalytic reaction. *Journal of Energy Chemistry*. **2021**, 52, 372–376.

[20] O Coufal, P Sezemsky and O Zivny, Database system of thermodynamic properties of individual substances at high temperatures. *J. Phys. D: Appl. Phys.* **2005**, *38*, 1265–1274.

[21] Baowei Wang, Wenjuan Yan, Wenjie Ge, Xiaofei Duan. Methane conversion into higher hydrocarbons with dielectric barrier discharge micro-plasma reactor. *Journal of Energy Chemistry.* **2013**, *22*, 876-882.

[22] Chao Xu, Xin Tu. Plasma-assisted methane conversion in an atmospheric pressure dielectric barrier discharge reactor. *Journal of Energy Chemistry.* **2013,** *22*, 22420–425.

[23] M. Scapinello, E. Delikonstantis, G.D. Stefanidis. Direct methane-to-ethylene conversion in a nanosecond pulsed discharge. *Fuel.* **2018**, *222*, 705–710.

[24] Faisal Saleem, Jonathan Kennedy, Usman H Dahiru, Kui Zhang, Adam Harvey. Methane conversion to $H_2$ and higher hydrocarbons using non-thermal plasma dielectric barrier discharge reactor. *Chemical Engineering & Processing: Process Intensification.* **2019**,*142*, 107557.

[25] E. Delikonstantis, M. Scapinello, O. Van Geenhoven, and G. D. Stefanidis, Nanosecond pulsed discharge-driven non-oxidative methane coupling in a plate-to-plate electrode configuration plasma reactor, *Chem. Eng. J*. **2020**, *380*, 122477.

[26] Galvita, V.; Siddiqi, G.; Sun, P.; Bell, A.T. Ethane dehydrogenation on Pt/Mg(Al)O and PtSn/Mg(Al)O catalysts. *J. Catal*. **2010**, 271, 209–219.

[27] Wegener, E.C.; Wu, Z.; Tseng, H.T.; Gallagher, J.R.; Ren, Y.; Diaz, R.E.; Ribeiro, F.H.; Miller, J.T. Structure and reactivity of Pt–In intermetallic alloy nanoparticles: Highly selective catalysts for ethane dehydrogenation. *Catal. Today* **2018**, 299, 146–153.

[28] Xie, Q.; Lei, T.; Miao, C.; Hua, W.; Yue, Y.; Gao, Z. Au/TiO2 for Ethane Dehydrogenation: Effect of Silica Doping. *Catal. Letters* **2020**, 150, 2013–2020.

[29] Rao, T.V.M.; Zahidi, E.M.; Sayari, A. Ethane dehydrogenation over pore-expanded mesoporous silica-supported chromium oxide: 2. Catalytic properties and nature of active sites. *J. Mol. Catal. A Chem.* **2009**, 301, 159–165.

[30] Nakagawa, K.; Kajita, C.; Ide, Y.; Okamura, M.; Kato, S.; Kasuya, H.; Ikenaga, N.O.; Kobayashiand, T.; Suzuki, T. Promoting effect of carbon dioxide on the dehydrogenation and aromatization of ethane over gallium-loaded catalysts. *Catal. Lett*. **2000**, 64, 215–221.

[31] Wang, L.C.; Zhang, Y.; Xu, J.; Diao, W.; Karakalos, S.; Liu, B.; Song, X.; Wu, W.; He, T.; Ding, D. Non-oxidative dehydrogenation of ethane to ethylene over ZSM-5 zeolite supported iron catalysts. *Appl. Catal. B Environ*. **2019**, 256, 117816.

[32] Z. Wu, B. C. Bukowski, Z. Li, C. Milligan, L. Zhou, T. Ma, Y. Wu, Y. Ren, F. H. Ribeiro, W. N. Delgass, J. Greeley, G. Zhang and J. T. Miller, Changes in Catalytic and Adsorptive Properties of 2 nm Pt3Mn Nanoparticles by Subsurface Atoms. *J. Am. Chem. Soc.*, **2018**, 140, 14870–14877.

[33] L. Wang, Y. Wang, C. W. Zhang, J. Wen, X. Weng and L. Shi, A boron nitride nanosheet-supported Pt/Cu cluster as a high-efficiency catalyst for propane dehydrogenation. *Catal. Sci. Technol.*, **2020**, 10, 1248–1255.

[34] L. L. Shen, K. Xia, W. Z. Lang, L. F. Chu, X. Yan and Y. J. Guo, The effects of calcination temperature of support on PtIn/Mg(Al)O catalysts for propane dehydrogenation reaction. *Chem. Eng. J.*, **2017**, 324, 336–346.

[35] A. WÈ©grzyniak, A. Rokicińska, E. HÈ©drzak, B. Michorczyk, K. Zeńczak-Tomera, P. Kuśtrowski and P. Michorczyk, High-performance Cr-Zr-O and Cr-K-O catalysts prepared by nanocasting for dehydrogenation of propane to propene. *Catal. Sci. Technol.*, **2017**, 7, 6059– 6068.

[36] X. Q. Gao, W. D. Lu, S. Z. Hu, W. C. Li and A. H. Lu, Rod-shaped porous alumina-supported Cr2O3 catalyst with low acidity for propane dehydrogenation. *Chin. J. Catal.*, **2019**, 40, 184–191.

[37] Y. Zhang, S. Yang, J. Lu, Y. Mei, D. He and Y. Luo, Effect of a Ce Promoter on Nonoxidative Dehydrogenation of Propane over the Commercial $Cr/Al_2O_3$ Catalyst. *Ind. Eng. Chem. Res.*, **2019**, 58, 19818–19824.

[38] K. M. Sundaram and G. F. Froment. Modeling of thermal cracking kinetics. 3. Radical mechanisms for the pyrolysis of simple paraffins, olefins, and their mixtures. Ind. Eng. Chem. Fundam. **1978**, 17, 174-182.